Supplementary Information (SI) for Journal of Materials Chemistry A.

Supporting Information

Deciphering the Local Structure of Prussian Blue Analogue Cathodes with Raman Spectroscopy for Sodium-ion Batteries

Krishnakanth Sada, Siddhartha Nanda, Hadi Khani, Arumugam Manthiram*

Materials Science and Engineering Program and Walker Department of Mechanical Engineering, The University of Texas at Austin, Austin, Texas 78712, USA.

Corresponding author. Tel: +1-512-471-1791

E-mail address: manth@austin.utexas.edu (A. Manthiram)

Supporting Note1

Experimental Details:

Raman Spectroscopy:

Raman spectra of the samples were collected with a Horiba LabRAM HR Evolution Raman spectrometer equipped with a 532 nm excitation laser, covering a Raman shift range from 100 to 3,100 cm^{-1}, with the laser power set between 2 and 3.15 mW. To ensure data reliability, the sample locations were optically examined after spectral acquisition, and repeat spectra were recorded to check for potential damage caused by localized heating; no damage was observed under these experimental conditions. The spectrometer configuration included a 600 lines/mm grating, a 200 μm pinhole, and an Olympus 50x LWD objective lens with a 10.6 mm working distance. Standard measurements consisted of five acquisitions, each lasting 30 s unless otherwise specified. For operando experiments, spectra were recorded at intervals of 5 to 10 minutes during continuous galvanostatic cycling. An ECC-Opto-Std optical cell (EL-CELL) was used, where the free-standing M-NFF and R-NFF cathodes faced the Raman spectrometer objective, while sodium metal or hard carbon served as the anode. The cell was connected to a LAND battery tester for galvanostatic cycling. An autofocus feature based on Raman spectral intensity, optimized along the Z-direction of the microscope, was employed at the start of each spectral acquisition, which proved beneficial for analyzing rough surfaces. Spectral preprocessing, including smoothing (using Gaussian and Lorentzian functions) and baseline correction (with a fifth-degree polynomial), was performed using LabSpec 6 software.

X-ray Photoelectron Spectroscopy:

X-ray photoelectron spectroscopy (XPS) measurements were conducted with a Kratos Analytical spectrometer equipped with monochromatic Al K_α radiation (1486.6 eV). Samples were transferred to the spectrometer with an airtight stainless-steel transfer vessel. The charge neutralizer was disabled to prevent alterations in peak positions and line shapes. The XPS samples were prepared carefully inside the glove box. The electrodes were extracted from the disassembled cells and washed three times with DEC solvent by soaking for 5 mins to remove the electrolyte residues from the surface.

Electrode preparation and electrochemistry:

The electrochemical cells were assembled with dry-cast electrodes. For the dry-cast electrodes, a mixture of active material, Ketjen black, and polytetrafluoroethylene (PTFE, Sigma) binder in a ratio of 8.5 : 1.0 : 0.5 was meticulously blended. The active material and Ketjen black were thoroughly mixed in a mortar and pestle for 30 min. Subsequently, PTFE binder was gradually added while gently mixing the powder, initiating the formation of a sheet. This sheet underwent multiple rolling and folding cycles to ensure a homogeneous composition, resulting in a well-structured electrode sheet. To attain densified electrodes, the sheets underwent hot calendaring, ensuring that the cathode active mass loading exceeded 8 - 10 mg cm^{-2} in both cases. It is crucial to emphasize that the entire dry-casting process was conducted inside a glove box to prevent exposure to air. Additionally, special care was taken during the calendaring of electrodes to minimize air exposure. The mass balancing for cathode and anode was calculated based on their theoretical capacities of, respectively, 150 and 270 mA h g^{-1}.

The electrodes were punched into 10 mm diameter disks. A sodium-metal anode, freshly prepared with a higher surface area compared to the working electrode, was achieved by rolling chunks of sodium metal. For full cell, we used commercial hard carbon anode, purchased from MTI, directly without any further modifications. Both the anode and cathode were separated by a Celgard separator (Grade 2325) and assembled into CR2032 coin cells inside an Ar-filled glove box, maintained at oxygen (O_2) and water (H_2O) levels of 0.1 ppm. A homemade electrolyte, consisting of 1 M $NaPF_6$ (sodium hexafluorophosphate, Alfa aesar 99+%) in a mixture of ethylene carbonate (EC; sigma 99%) and diethyl carbonate (DEC; sigma 99%) in a 1:1 volume ratio with 3 wt.% fluoroethylene carbonate (FEC), was used for fabrication of all the cells. 30 - 50 μL of electrolyte was used for each cell. For all ex-situ samples, coin cells with dry-cast electrodes were assembled. After cycling to specific charged or discharged states, these cells were disassembled, and the electrodes were thoroughly washed with an excess amount of DEC solvent for further analysis. The cells were tested with 1C = 150 mA g^{-1}. All the electrochemical tests were carried out at room temperature.

Pre-sodiation Strategy: Fresh sodium metal was prepared by rolling chunks of sodium-metal cubes. A commercial hard carbon anode, purchased from MTI, was directly placed in contact with sodium metal, with a drop of electrolyte facilitating the interface. A 250 g metal block was applied to the electrode for three minutes to unsure a uniform sodiation. Afterward, the electrode was removed and washed with the same electrolyte. The pre-sodiated electrodes were then used for full-cell assembly to mitigate the first-cycle irreversibility of the anode.

Synthesis of cathode materials:

$Na_2Fe[Fe(CN)_6]$ was synthesized through a simple and modified acid-based decomposition of sodium ferrocyanide decahydrate ($Na_4Fe(CN)_6$. $10.H_2O$) in a controlled manner. To begin the process, 4 mmols of sodium ferrocyanide was introduced into 0.1 M hydrochloric acid solution under a nitrogen environment and maintained at 80 °C. The mixture was stirred continuously for several hours, during which a gradual transition to light blue color was observed, indicating initial phase formation. The solution was then left to age around 5 h before the introduction of sodium iodide. Subsequent stirring for an additional 5 h ensured complete reaction. The resulting product was cleaned twice with a water-ethanol mixture and finally rinsed with pure ethanol to promote efficient drying. The material was then vacuum-dried overnight at 80 °C, yielding a pale blue powder with monoclinic crystal structure. It was then dried under vacuum at 180-200 °C to remove interstitial water molecules.

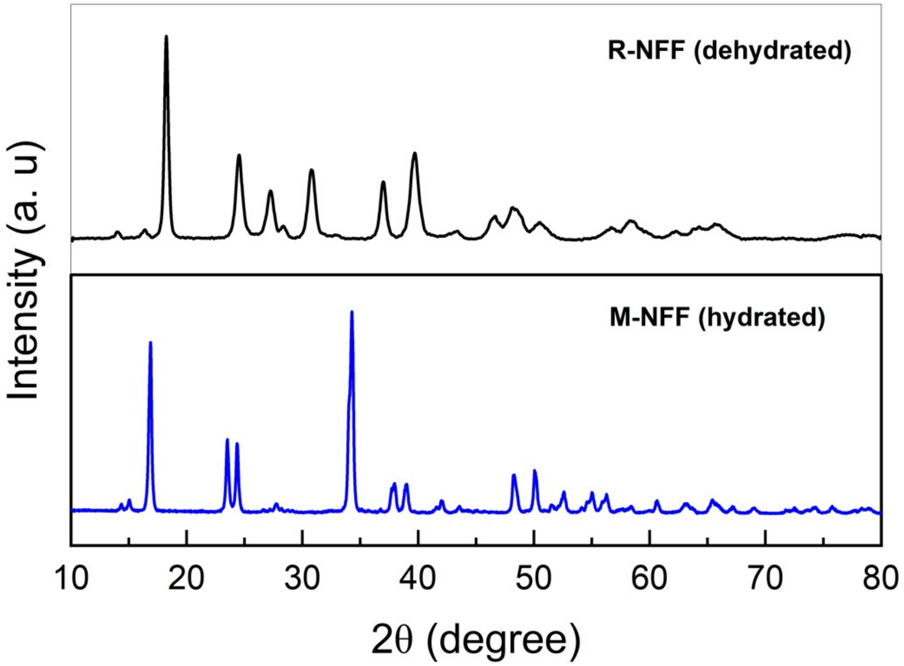

Fig S1: Comparison of the X-ray diffraction patterns of both the hydrated and dehydrated sodium iron hexacyanoferrate.

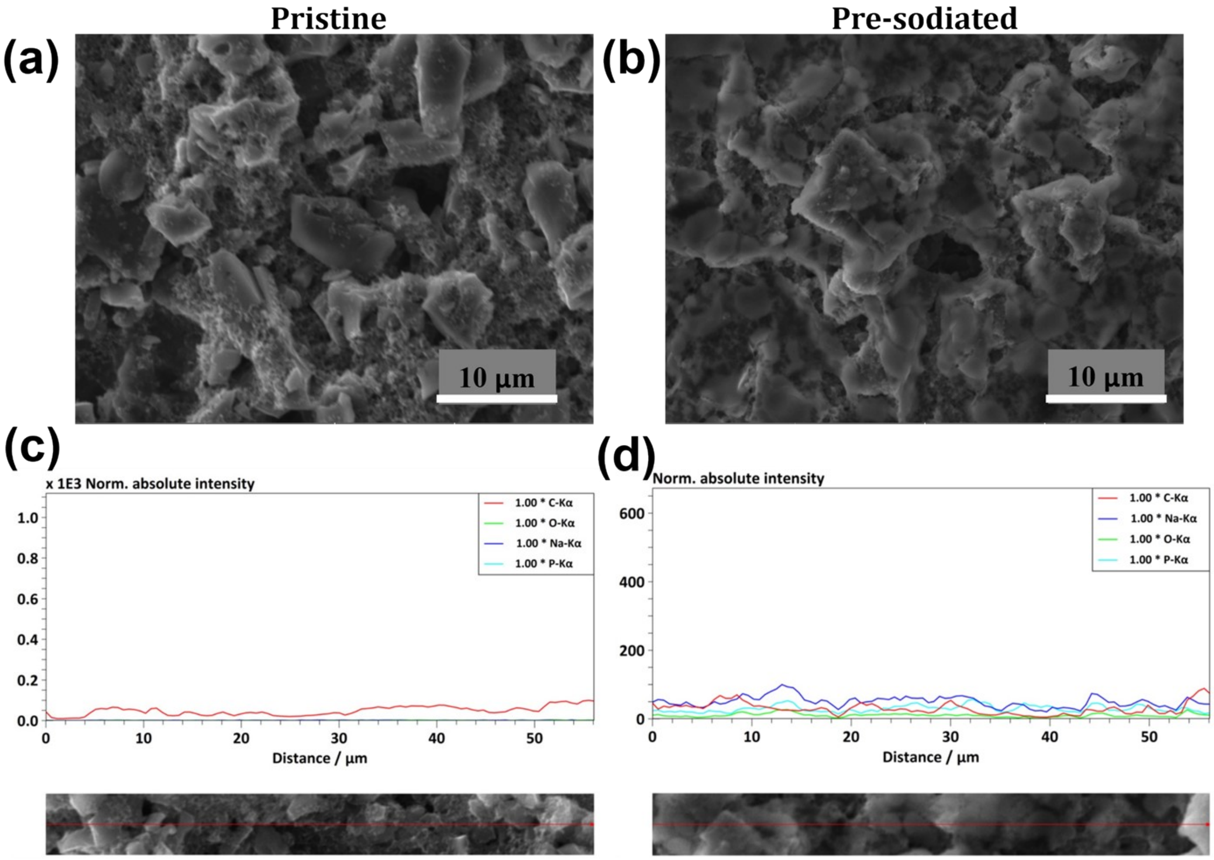

Fig S2: Comparison of (a) pristine and (b) pre-sodiated electrodes, highlighting the smoother surface morphology of the pre-sodiated electrodes compared to the pristine one. Energy-dispersive spectroscopy (EDS) analysis of the (c) pristine electrode reveals the presence of carbon, whereas (d) the pre-sodiated electrode is covered with components of the solid electrolyte interphase (SEI), indicating surface modification due to pre-sodiation.

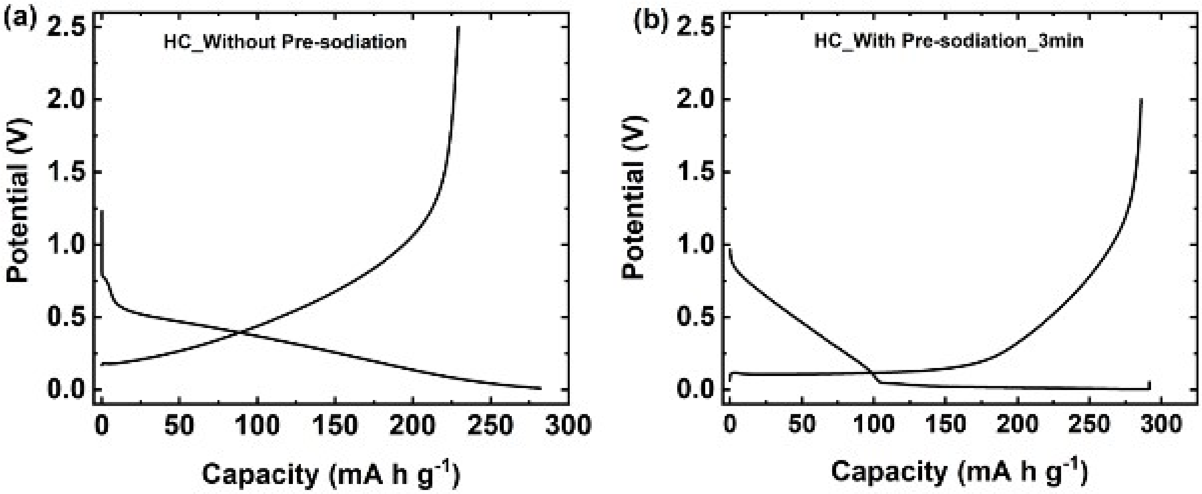

Fig S3: First cycle coulombic efficiency of hard carbon improving with the pre-sodiation strategy: (a) Galvanostatic charge-discharge of hard carbon without pre-sodiation and (b) cycling of hard carbon with pre-sodiation at C/10 rate.

Supporting note2

Potentiostatic intermittent titration was conducted at an extremely slow rate of C/50, with a 5 mV voltage pulse, followed by a 1-hour rest period to investigate the reaction mechanism. Careful consideration was given to each experimental parameter to minimize errors. The electrodes were prepared as densified free-standing films to address diffusion limitations. The insertion mechanisms for the half-cell and full-cell configurations varied within the lower voltage plateaus. In the half-cell configuration, both plateaus (3.35 V during charge / 3.27 V during discharge and 3.15 V during charge / 2.98 V during discharge) showed variations in current responses, as demonstrated in our earlier studies.[1] In contrast, the R-NFF full-cell configuration exhibited responsive current variation at higher voltage plateaus (3.2 V), but not within the lower voltage region, which showed a sloppy profile.

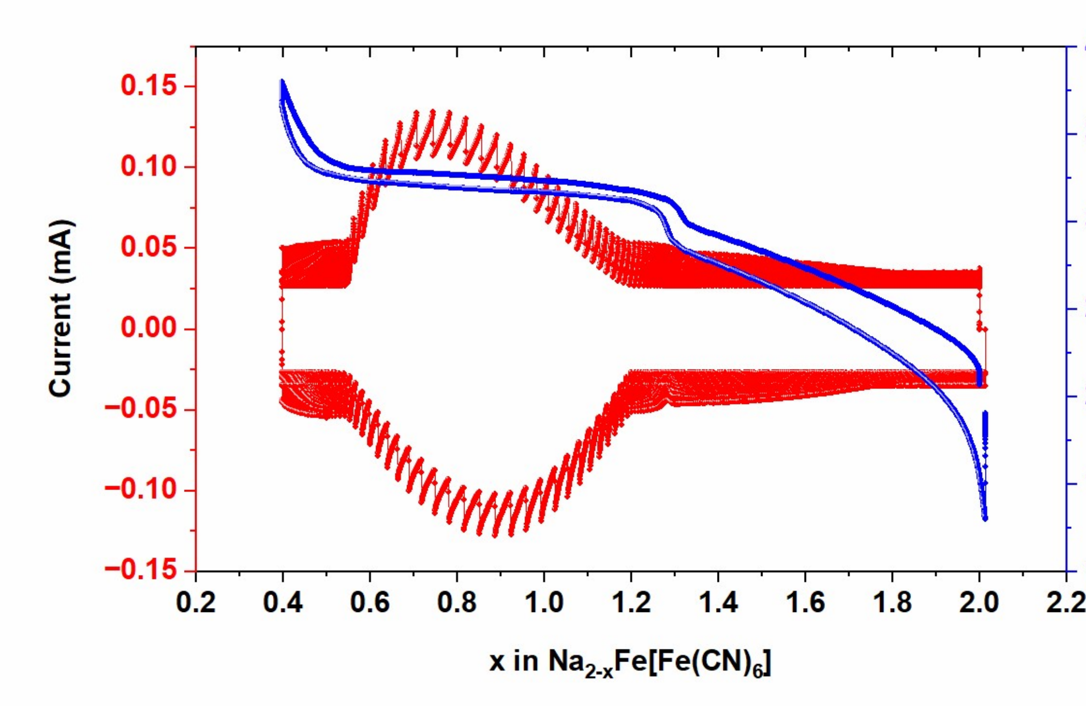

Fig S4. PITT curves for R-NFF full cell configuration, with current response exhibited at x = 1.2 to 0.5 (bell shape curve).

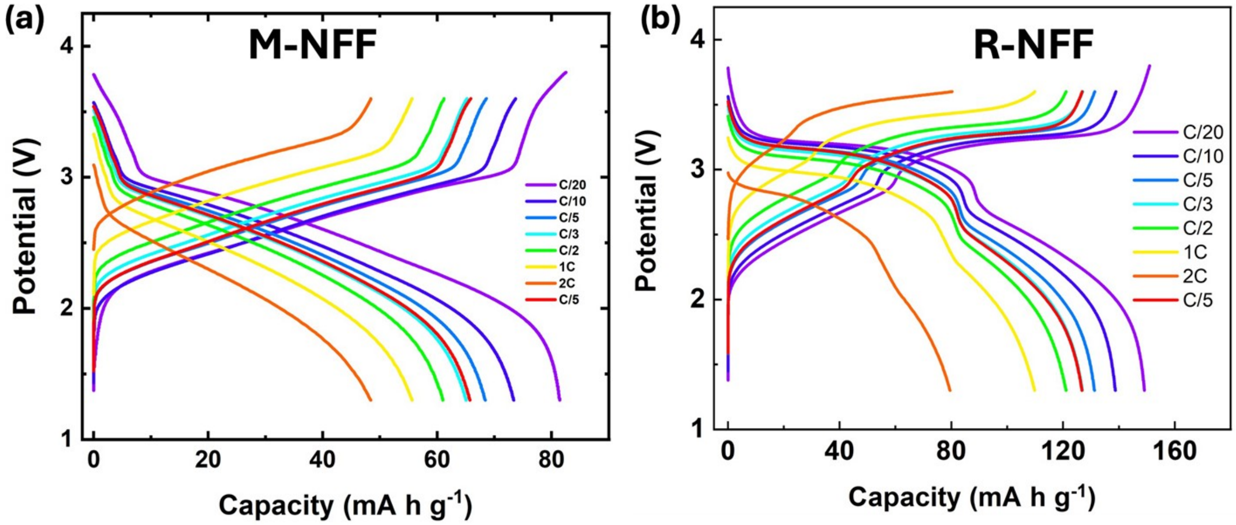

Fig S5. Charge-discharge profiles in the second cycle at different rates of C/20 to 2C.

Supporting note3.

The structure factor (F_h) of an atom depends on the atomic form factor (f), which is influenced by the scattering angle, atomic number, and X-ray wavelength. When using a copper (Cu) X-ray source, the wavelength is typically $\lambda = 1.5418\ \text{A}^\circ$ (K_α line). We can calculate the structure factor using the atomic form factors for C (carbon), N (nitrogen), and Fe (iron) for the given range of scattering angles $2\theta = 10° - 80°$

The **scattering vector (*q*)** is given by:

$$q = \frac{4\pi\ sin\theta}{\lambda}$$

The **atomic form factor (*f*)** varies with q and can be expressed as:

$$f(q) = \sum_{i=1}^{4} a_i e^{-b_i q^2} + c$$

where a_i, b_i, and c are tabulated constants for each element. These values are well-documented for C, N, and Fe in the International Tables for Crystallography.

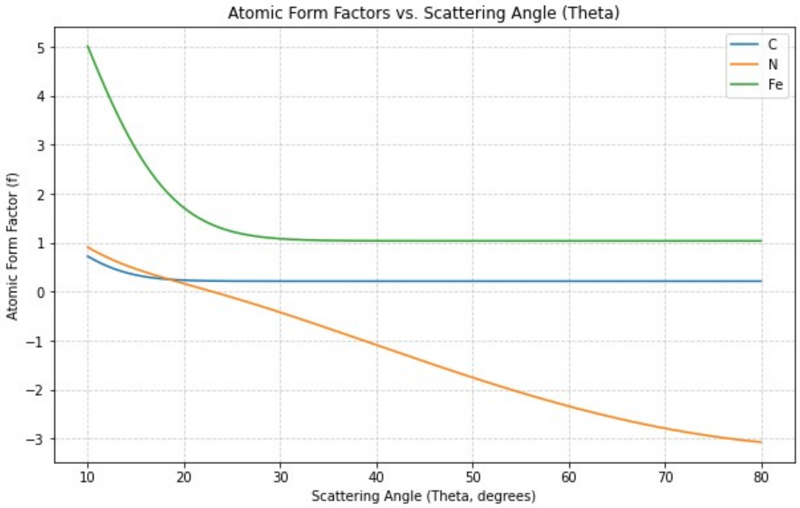

Fig S6. Atomic form factor *vs*. scattering angle plot demonstrates that the overall atomic form factor of carbon (C) and nitrogen (N) are significantly lower compared to that of iron (Fe), indicating their weaker X-ray scattering contributions and low sensitivity.

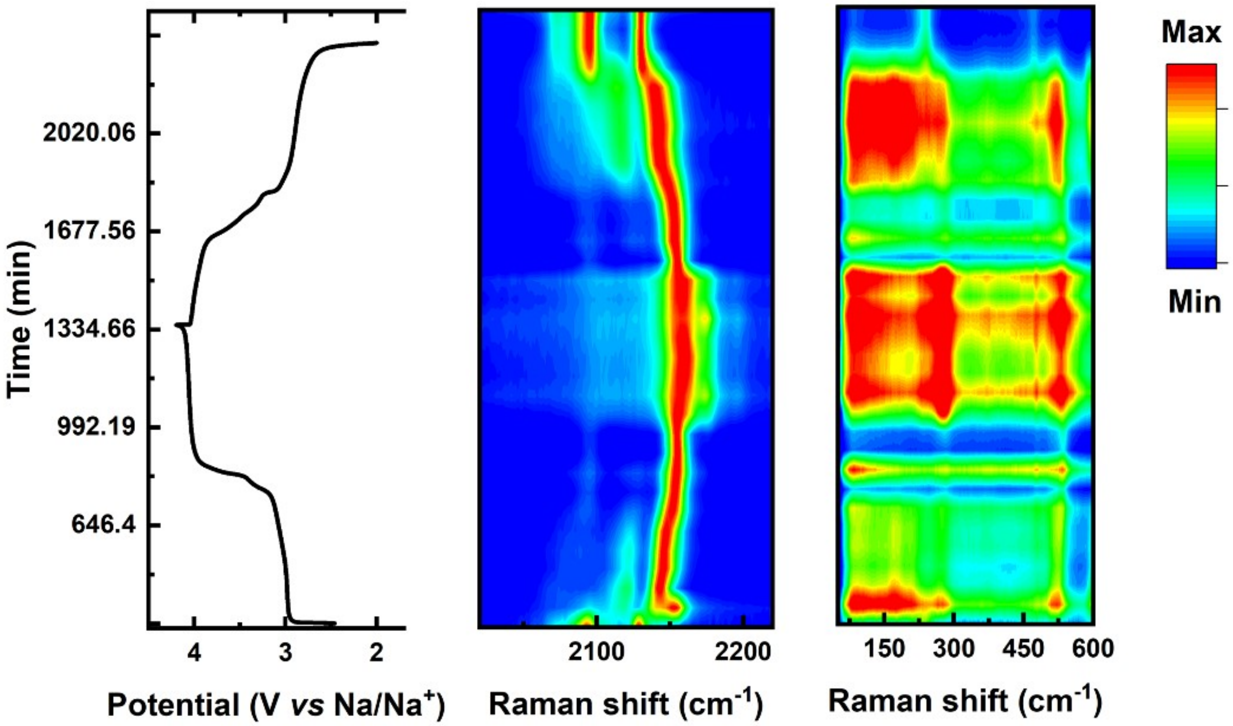

Fig S7. *Operando* Raman Spectroscopy of M-NFF in the first cycle.

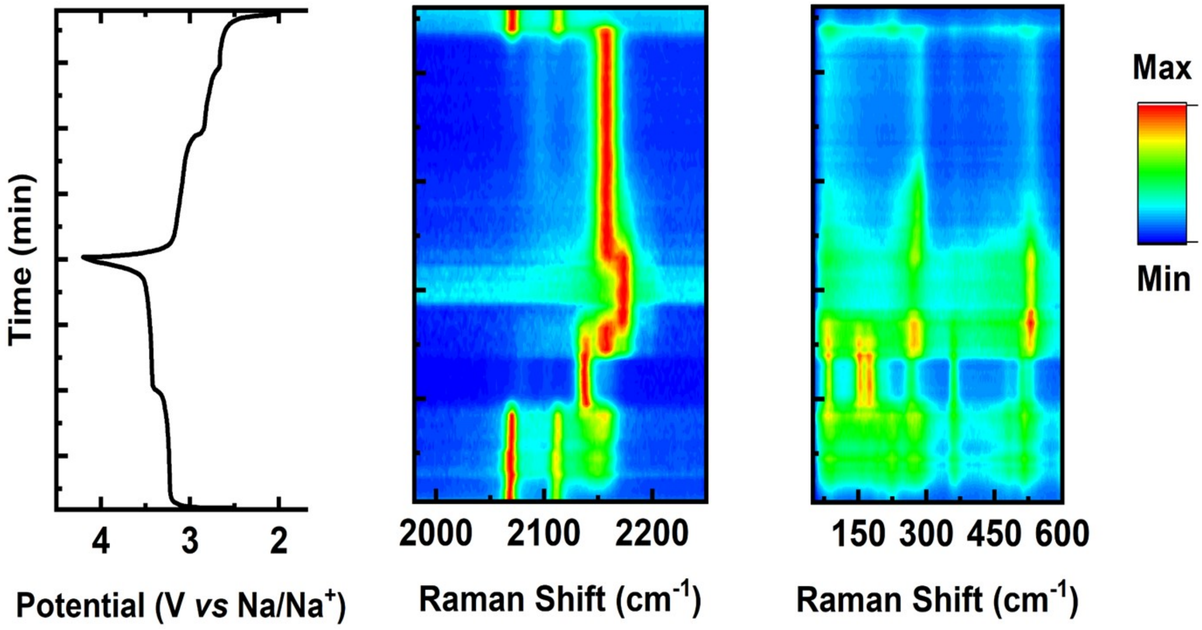

Fig S8. *Operando* Raman Spectroscopy of R-NFF in the first cycle.

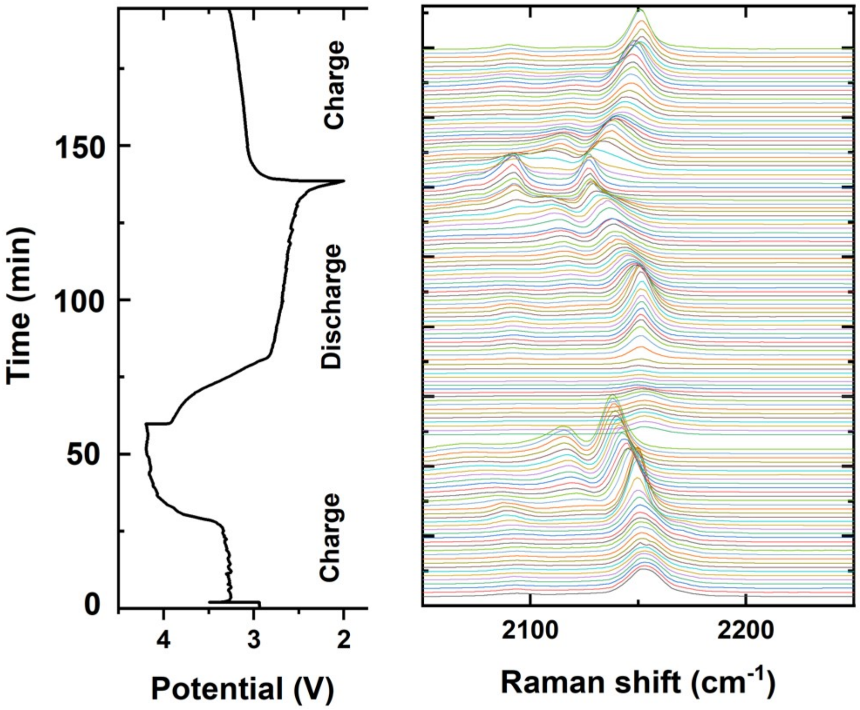

Fig S9. *Operando* Raman Spectroscopy of M-NFF after 100 cycles.

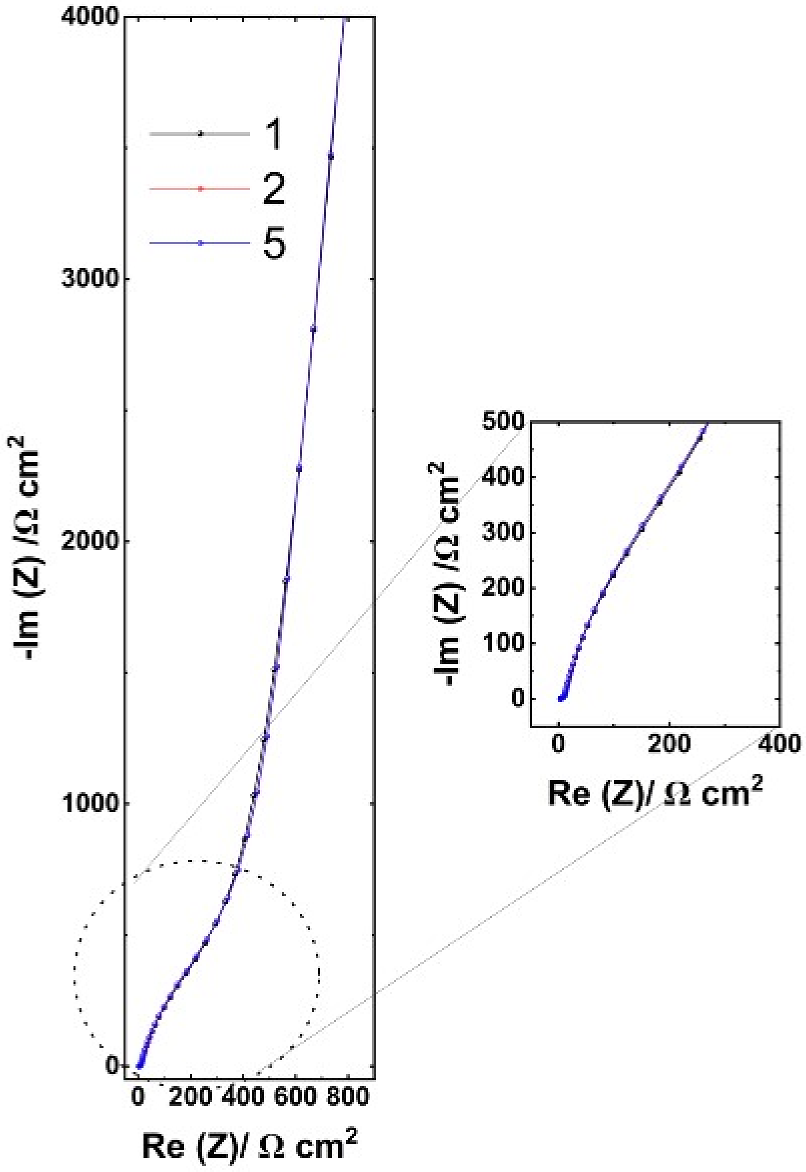

Fig S10. Impedance spectra of hard carbon in a symmetric cell configuration. Pristine hard carbon vs. charged hard carbon. It confirms that the resistance at the interface does not change drastically. We have compensated this resistance while calculating the operando EIS.

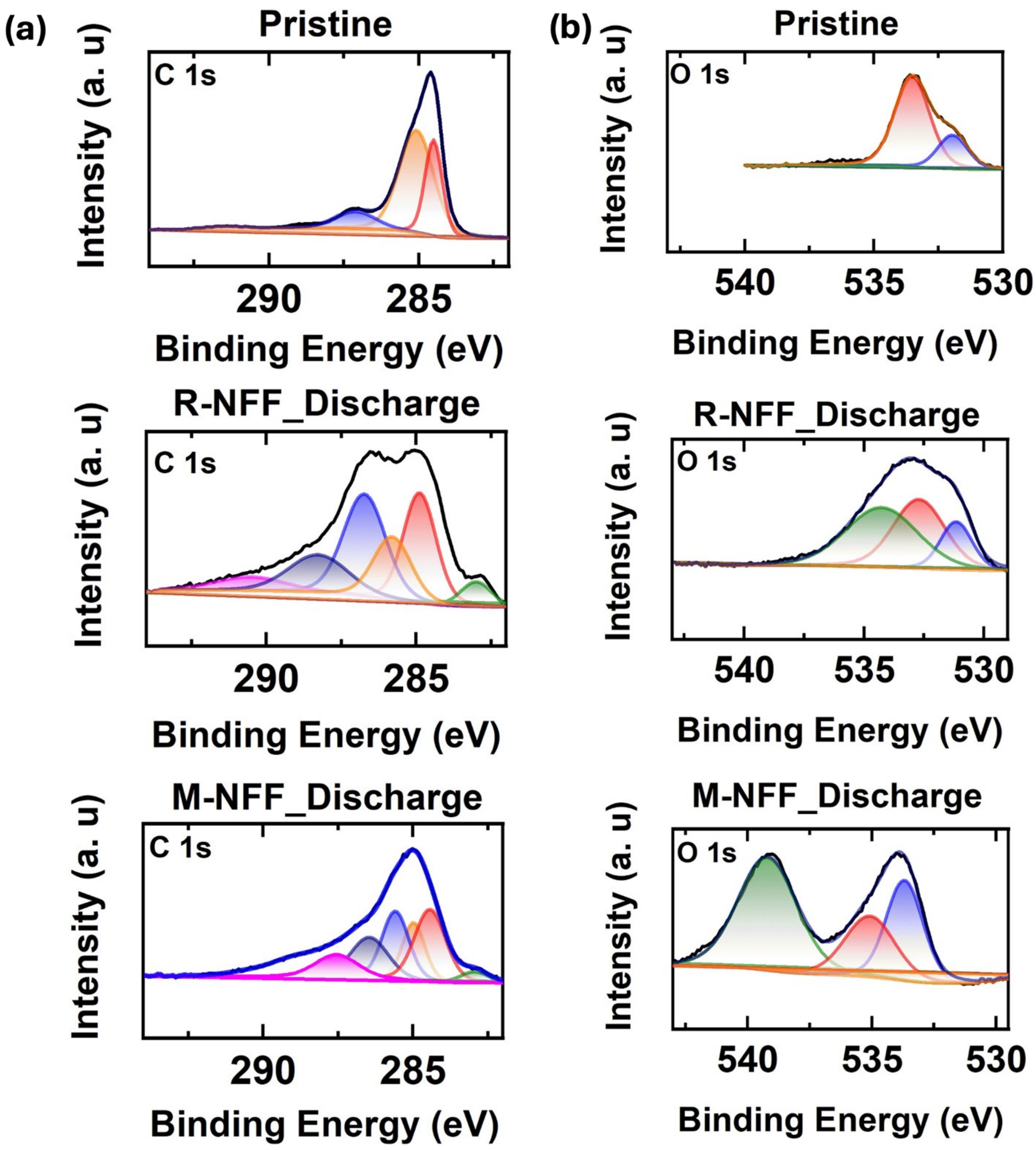

Fig S11. XPS C1s and O1s spectra of hard carbon, collected with respect to the pristine and discharged states of both R-NFF and M-NFF.

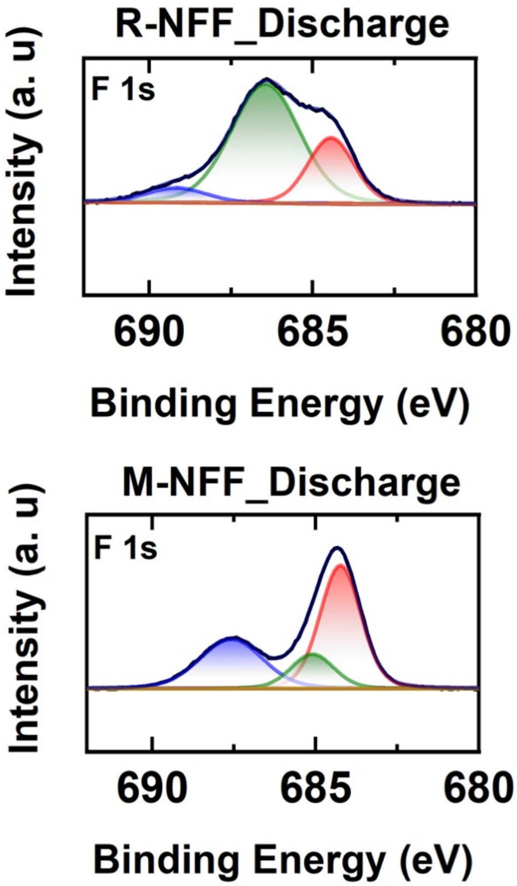

Fig S12. XPS F1s spectra of hard carbon, collected with respect to the discharged states of both R-NFF and M-NFF.

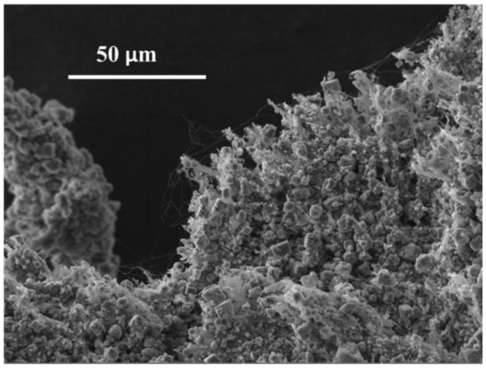

Fig S13. Scanning electron microscopy image of the self-standing electrode, showing the polymer forming a gabion-like structure to hold the cathode particles together.

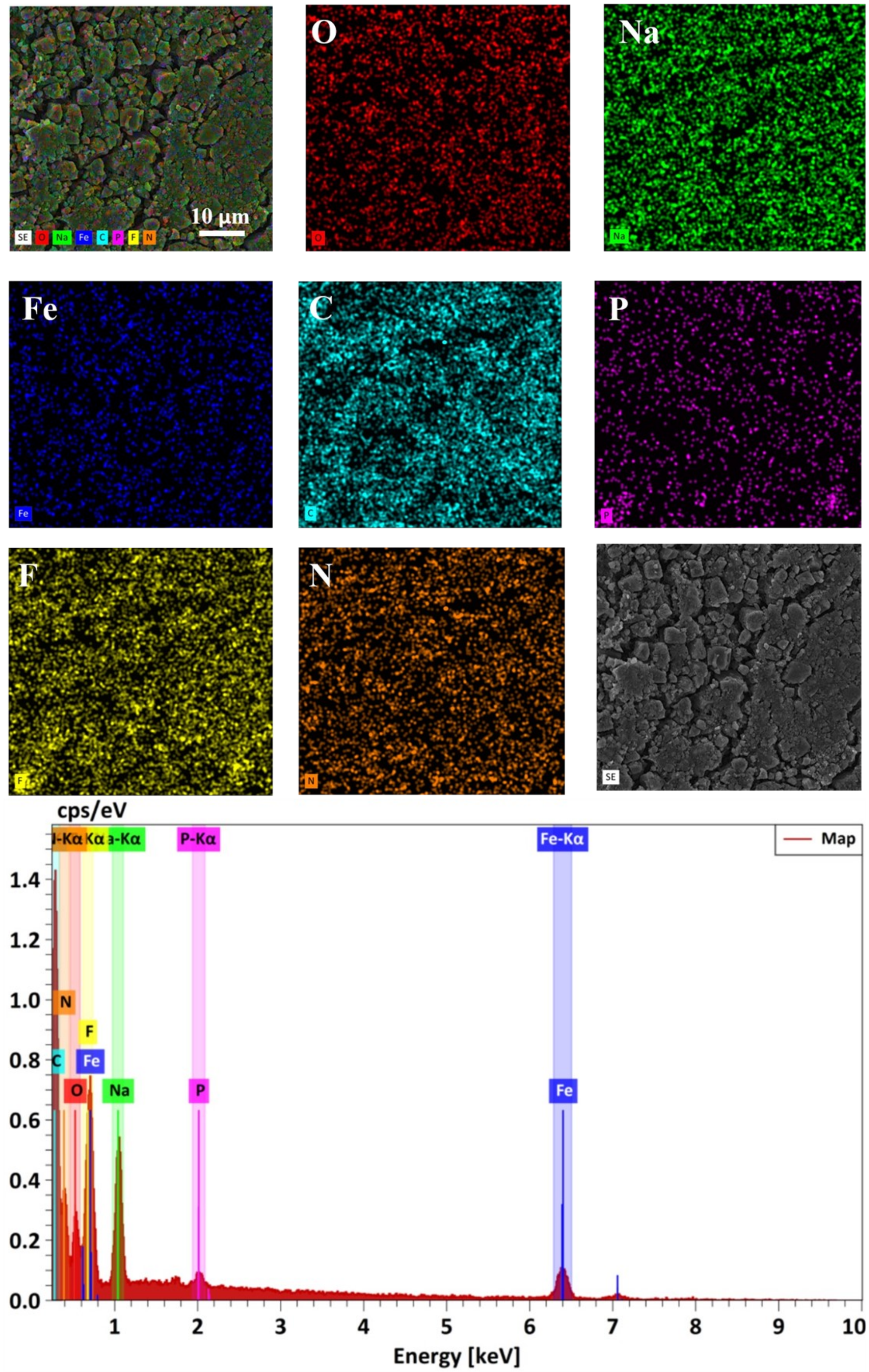

Fig S14. Elemental mapping and energy-dispersive spectra (EDS) of M-NFF electrodes after cycling.

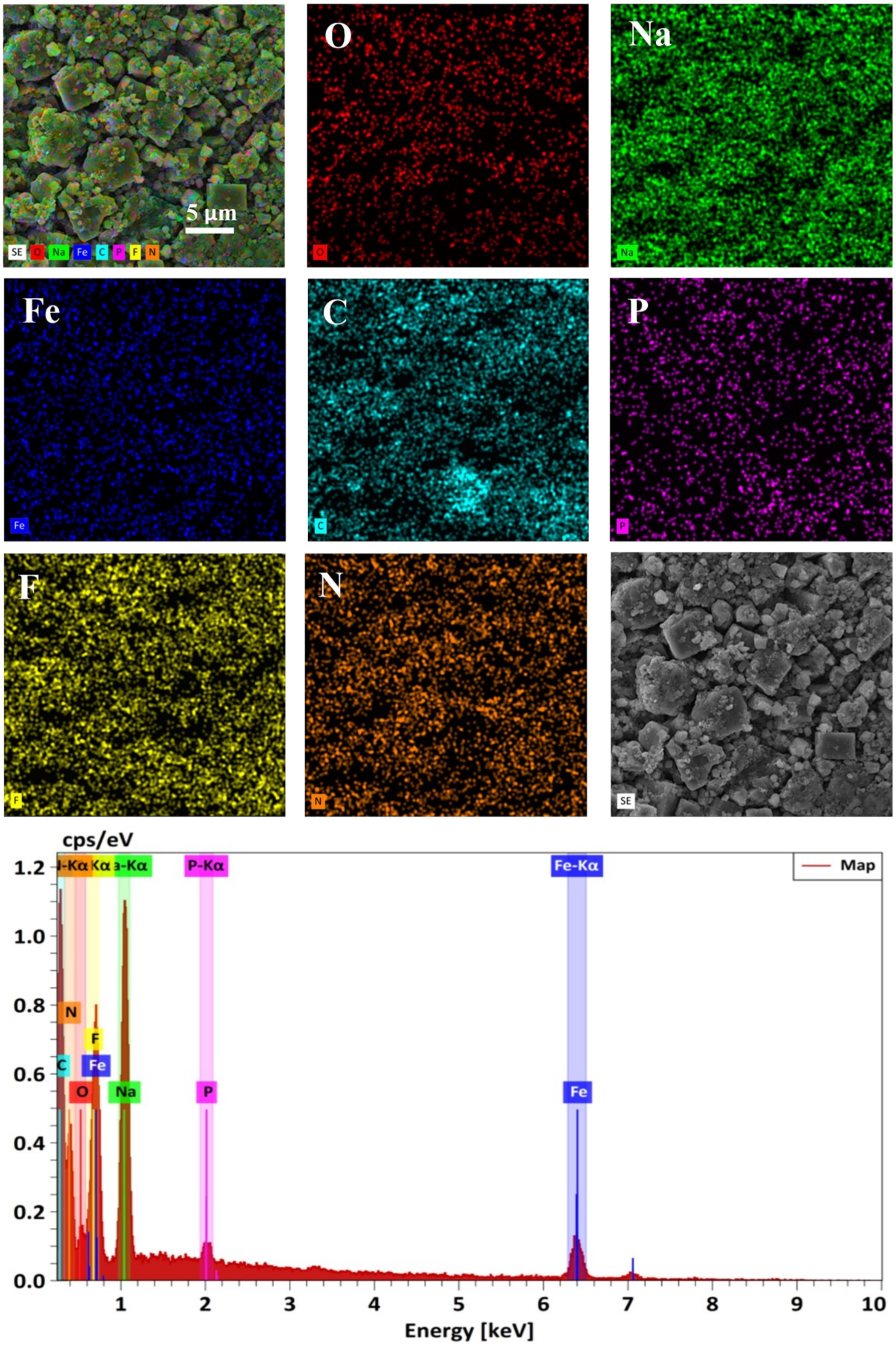

Fig S15. Elemental mapping and energy-dispersive spectra (EDS) of R-NFF electrodes after cycling.

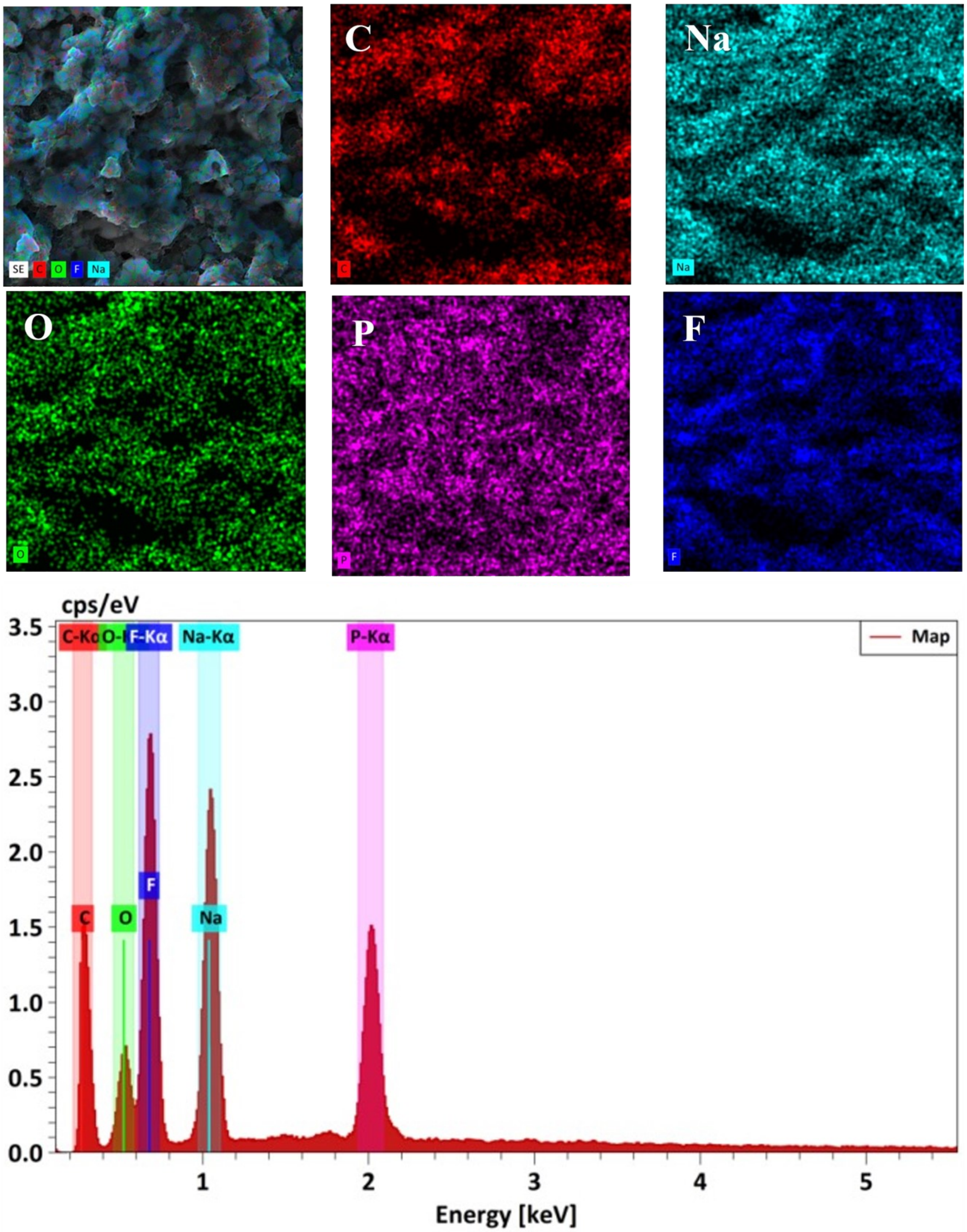

Fig S16. Elemental mapping and energy-dispersive spectra (EDS) of HC-anode electrode after pre-sodiation.

Supporting note 3:

It is important to understand the basics involved in the analysis of Raman spectra. The calculations of normal modes were carried out for O_h symmetry. Below is the simple representation of the octahedral AB_6 geometry:

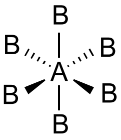

N_i = number of atoms that remain unshifted by the operation
χ_i = Sum of all the characters in the character table under the operation for the irreducible representations by which all 3-unit vectors transform.

Table S1. Characteristic table

O_h	E	$8C_3$	$6C_2$	$6C_4$	$3C_2$	i	$6S_4$	$8S_6$	$3\sigma_h$	$6\sigma_d$	h=48	
N_i	7	1	1	3	3	1	1	1	5	3		
χ_i	3	0	-1	1	-1	-3	-1	0	1	1		
Γ_{3n}	21	0	-1	3	-3	-3	-1	0	5	3	Σ	ni
A_{1g}	21	0	-6	18	-9	-3	-6	0	15	18	48	1
A_{2g}	21	0	6	-18	-9	-3	6	0	15	-18	0	0
E_g	42	0	0	0	-18	-6	0	0	30	0	48	1
T_{1g}	63	0	6	18	9	-9	-6	0	-15	-18	48	1
T_{2g}	63	0	-6	-18	9	-9	6	0	-15	18	48	1
A_{1u}	21	0	-6	18	-9	3	6	0	-15	-18	0	0
A_{2u}	21	0	6	-18	-9	3	-6	0	-15	18	0	0
E_u	42	0	0	0	-18	6	0	0	-30	0	0	0
T_{1u}	63	0	6	18	9	9	6	0	15	18	144	3
T_{2u}	63	0	-6	-18	9	9	-6	0	15	-18	48	1

$\Gamma_{3n} = A_{1g} + E_g + T_{1g} + T_{2g} + 3T_{1u} + T_{2u}$

$\Gamma_{trans} = T_{1u}$ $\Gamma_{rot} = T_{1g}$ $\Gamma_{3n-6} = A_{1g} + E_g + T_{2g} + 2T_{1u} + T_{2u}$

Table S2: XPS parameters for $Na_2Fe[Fe(CN)_6]$, including the maximum binding energies (BE) of Fe^{2+} and Fe^{3+} $2p_{3/2}$ peaks, spin-orbit splitting (ΔBE_1) of the Fe 2p doublet, binding energy of the Fe $2p_{3/2}$ satellite peak, peak separation between the main Fe $2p_{3/2}$ and its corresponding satellite peaks (ΔBE_2), and the intensity ratio (I_ratio) of the main Fe $2p_{3/2}$ peak to its satellite peak.

SOC	**BE Fe^{II} 2p 3/2 main /eV**	**BE Fe^{III} 2p 3/2 main. /eV**	**$\Delta BE_1{}^a$/ eV**	**$\Delta BE_2{}^b$/ eV**	**$I_{ratio}{}^d$**	**BE Fe 2p 3/2 main /eV**	**BE Fe^{II} 2p 3/2 satel /eV**	**$\Delta BE_3{}^c$ / eV**	**$I\_{ratio\ satel}{}^e$**
R-NFF									
1 Pristine	708.5	709.3	12.85	0.8	1.33	708.7	711.1	2.4	0.74
2 Charge	708	708.7	12.91	0.7	1.12	708.2	712.9	4.7	0.84
3. Discharge	708.3	709.3	12.85	1.2	1.34	708.5	713.8	5.3	0.78
M-NFF									
4. Pristine	708.7	709.5	12.77	0.73	1.50	708.7	711.4	2.7	0.64
5. Charge	708.4	708.7	12.85	0.31	1.13	708.4	713.5	5.1	0.81
6. Discharge	708.6	709.6	12.76	1.05	1.47	708.6	712.3	3.7	0.67

[a] $\Delta BE_1 = BE_{Fe\ 2p1/2main} - BE_{Fe\ 2p3/2\ main}$

[b] $\Delta BE_2 = BE_{Fe^{3+}\ 2p3/2main} - BE_{Fe^{2+}\ 2p3/2\ main}$

[c] $\Delta BE_3 = BE_{Fe\ 2p3/2\ satel} - BE_{Fe\ 2p3/2\ main}$

[d] I_{ratio} = Ratio between the intensities of the Fe^{2+} and Fe^{3+} Fe $2p_{3/2}$ peaks ($I_{ratio} = (I_{FeII\ 2p3/2\ main})/(I_{FeIII\ 2p3/2\ main})$).

[e] $I_{ration\ satel}$ = ratio between the intensities of the satellite and main Fe 2p3/2 peaks ($I_{ratio} = (I_{Fe2p3/2\ satel})/(I_{Fe2p3/2\ main})$)

References

1. Sada, K.; Greene, S. M.; Kmiec, S.; Siegel, D. J.; Manthiram, A. Unveiling the Influence of Water Molecules on the Structural Dynamics of Prussian Blue Analogues. *Small* **2024**, *20* (50). https://doi.org/10.1002/smll.202406853.